Journal Pre-proof

Exploring the potential of branched submicron channels-based structures in ultra-thin Ag films for SERS molecular sensing

Simón Roa , María José Cortés Burgos , María Laura Pedano

Please cite this article as: Simón Roa , María José Cortés Burgos , María Laura Pedano , Exploring the potential of branched submicron channels-based structures in ultra-thin Ag films for SERS molecular sensing, *Surfaces and Interfaces* (2023), doi: https://doi.org/10.1016/j.surfin.2023.103756

This is a PDF file of an article that has undergone enhancements after acceptance, such as the addition of a cover page and metadata, and formatting for readability, but it is not yet the definitive version of record. This version will undergo additional copyediting, typesetting and review before it is published in its final form, but we are providing this version to give early visibility of the article. Please note that, during the production process, errors may be discovered which could affect the content, and all legal disclaimers that apply to the journal pertain.

Exploring the potential of branched submicron channels-based structures in ultra-thin Ag films for SERS molecular sensing

Simón Roa[1]*, María José Cortés Burgos[1], María Laura Pedano[1,2]*

[1]Instituto de Nanociencia y Nanotecnología (CNEA - CONICET), Nodo Bariloche, Consejo Nacional de Investigaciones Científicas y Técnicas (CONICET) and Centro Atómico Bariloche (CAB), Comisión Nacional de Energía Atómica (CNEA), Av. E. Bustillo 9500, R8402AGP San Carlos de Bariloche, Río Negro, Argentina.
[2]Instituto Balseiro, CNEA-Universidad Nacional de Cuyo (UNCUYO), Av. E. Bustillo 9500, R8402AGP San Carlos de Bariloche, Río Negro, Argentina.

(*) Corresponding authors e-mails: sroadaz8@gmail.com **(S. Roa),** ml.pedano@cab.cnea.gov.ar **(M. L. Pedano)**

Abstract

Noble metal-based nanostructures are actively studied due to their promising prospects for fabricating efficient substrates for Surface Enhanced Raman Spectroscopy (SERS)-based molecular sensing. In this work, we report the gross potential of SERS substrates based on branched submicron channels in ultra-thin Ag films. These films were fabricated by magnetron sputtering and then annealed in high vacuum conditions to induce branched channels growth by thermal dewetting. Different sets of nominally equal samples were tested during a determined period of time, using confocal Raman spectroscopy and methylene blue (MB) as Raman-active molecule, to assess their performance for SERS in ambient aging conditions. Micro-Raman intensity mapping studies demonstrated the emergence of "hot spots" enhancing the Raman signal in the branched submicron channels. A good mass sensitivity and fast spectral acquisition were achieved using these nanostructures, observing an exceptional spectral resolution, in a few seconds, in samples with a MB surface mass density of about 2 [ng/mm^2]. A good spectral resolution was achieved even using shorter measurement times from 1.00 to 0.05 second, suggesting the potential for fast SERS determinations. Samples showed good reproducibility in the Raman spectral response during the tested period, demonstrating the marginal impact of the aging effects on the Raman signal enhancement and ensuring a time-stable SERS performance in the short term. Our results show that the proposed nanostructures are promising candidates for the development of substrates with competitive-sensitivity, time-stability, and fast SERS response, representing a simple and attractive alternative for efficient SERS-based molecular sensing.

Keywords: Molecular Sensing, Surface-Enhanced Raman Spectroscopy, Nanostructured Plasmonic Materials, Noble Metal Thin Films.

1. Introduction

Surface-enhanced Raman scattering is a surface-sensitive molecular scattering process where adsorbed molecules onto nanostructured metal surfaces can scatter and tremendously amplify the incident light intensity by geometry-induced electric field enhancement mechanisms [1]. It is an inelastic scattering process that modifies the incoming light wavelength, revealing the vibrational signature of the adsorbed molecules. Raman scattering is a low-probability physical process, about one photon out of a million incident photons. Nevertheless, the presence of metal-enhanced electric-near fields that arise due to the Surface Plasmon Resonance (SPR) at the metal-dielectric interface can make this scattering process very efficient [2]. Molecular scattering cross-section increases by manifold due to SPR near-fields, which can make scattering strength as large as 10^{10} times the signal measured with simple backscattered geometry from molecules/analytes on planar substrates [3]. Surface-Enhanced Raman Spectroscopy (SERS) has been extensively used as a high-sensitivity sensing technique of the vibrational states (or vibrational spectral signature) of a wide variety of organic and inorganic molecules with relevance in different areas of chemistry and biology [4 − 6]. SERS is a highly selective technique that enables the detection of small amounts of specific molecules by the measurement of their vibrational spectra (Raman spectral signature), which is unique for each one and depends on the nature of the molecular structure, for example, elements and geometry of the chemical bonds.

In recent years, many efforts have been focused on fabricating and studying different kinds of SERS substrates based on micro/nanostructured noble metal surfaces. This is due to their promising prospects for high-sensitivity molecular detection by the emergence of localized plasmonic "hot spots" [7 − 15], which act as local Raman signal amplifiers. Au and Ag nanostructures have been the most studied and popularly used metals due to their low

reactivity, good air stability, and exceptional plasmonic activity for visible/near-infrared light which are the typical wavelengths required for SERS-based molecular sensing [3]. Nowadays, Au nanostructures are generally preferred for SERS applications because of their exceptionally inert chemical nature and long-term stability (oxidation resistance, for example) [16 − 18]. Nevertheless, Ag-based nanostructures have become relevant in this area due to their gross potential for fabricating low-cost and efficient SERS substrates, which lies in the considerably higher plasmonic efficiency [16, 18] and lower price of Ag concerning Au (in the order of 800 USD/kg compared with 62000 USD/kg for Au, Daily Metal Price: Copper Price (USD / Pound) Chart for the Last Month). Many studies have demonstrated the potential of different kinds of Ag nanostructures for high-sensitivity, fast-acquisition, and/or time-stable SERS-based molecular sensing [16 − 26]. In this context, these have found applications in different areas with potentially high impact in society demands like detection of micro-organisms (*S. aureus* and *E. coli*) for disease diagnostics [16], water pollutants associated with pharmaceuticals for human-consumption water control [18], pesticides and organic pollutants in agriculture products [22, 23], biomolecules (adenine) and organic water pollutants (for example, methylene blue and malachite green) [24, 26], uremic toxins (creatinine, uric acid, and urea) and parathyroid hormone [25], etc. Thus, different studies continue being proposed looking for competitive Ag-based sensing nanostructures with reasonably good performance-costs relations and industrial scalability prospects for SERS-based molecular sensors.

Many nanofabrication techniques like Physical Vapor Deposition (PVD), Interference Laser Lithography (ILL), Focused Ion Beam (FIB), Electron-Beam Lithography (EBL), and chemical-based methodologies have been used to fabricate a wide variety of plasmonic-active metallic nanostructures [3]. Procedures based on nanolithography processes (FIB, EBL, and ILL) are generally used to fabricate more complex structures and control different geometrical

parameters with high accuracy for efficient SERS performance management. However, these are usually difficult and expensive to implement, and considerably time-consuming. Therefore, current scientific community attention is strongly focused on exploring and studying simple, low-cost, industrially scalable, and easily reproducible technical strategies to fabricate efficient and competitive SERS substrates, as well as on the use of other low-cost plasmonic-active metals like Ag [16 – 26].

In this work, we report the gross potential of SERS substrates based on branched submicron channels in ultra-thin Ag films fabricated by thermally-induced dewetting in high vacuum conditions. Here, we show preliminary novelty in the fabrication of a particular kind of Ag nanostructure that enables high-resolution, fast, and reproducible SERS-based molecular sensing performance. Moreover, unlike most similar studies, we report consistent evidence of the advantages of our samples to achieve high and reproducible Raman spectral resolution with a fast response rate over short-term aging effects on the sample surface. Methylene Blue (MB) was used as a Raman marker to assess the performance of our samples for SERS-based molecular sensing. MB is commonly used in medical practice as a dye in microbiological staining and drug in treatments for Methemoglobinemia, dermatological diseases, etc [27 – 29]. It is also a common water pollutant derived from textile and food industry processes, and its detection is a key issue in water quality controls [30 – 32]. Due to its biological and industrial relevance, much attention has been focused on developing detection methods of MB. Our results show that the proposed nanostructures are promising candidates for designing competitive-sensitivity, time-stable, and fast SERS substrates, representing a simple and attractive alternative for efficient SERS-based molecular sensing.

2. Experimental details

2.1. Thin films fabrication. Ag thin films were fabricated on commercial soda-lime glass substrates by Direct Current (DC) sputtering using a 108 Auto Sputter Coater (from *TED PELLA, INC.*), as shown in **Fig.1**. An Ar pressure of 0.08 [mbar] and a current of 40 [mA] were set as nominal deposition conditions to achieve a

deposition rate of 0.9 [nm/s] and homogeneous 23 [nm]-thick Ag thin films (approx. 25 [s] of deposition time). Each sample consists of a 2 x 2 array of 23 [nm]-thick Ag thin films deposited on a square soda-lime glass substrate of 12.7 [mm] x 12.7 [mm], as schemed in **Fig. 1** for the ideal sample geometry in the step 1. This array was printed on the substrate during the sputtering process by using a homemade PET mask previously fabricated with the desired design. Four of these samples were consecutively fabricated on the same day.

2.2. Annealing treatments. Ag thin film dewetting mechanism was thermally induced by using a homemade high-vacuum annealing system (work pressure < 10^{-3} [Torr]). This system consists of a high-temperature tubular oven coupled with a diffusion pump-assisted vacuum glass flask (the sample holder), as schemed in **Fig. 2** for step 2. The four samples were simultaneously annealed at 773 K for 15 [min] with a heating rate = 5 [°C/min] to fabricate a complex disordered matrix of branched submicron channels. These annealing conditions were selected following those optimized in our previous work [33]. In that research, we empirically studied the effects of different Ag film thicknesses and post-annealing conditions on their microstructure evolution, obtaining a wide variety of microstructures like disordered nanoholes, micro and nanoparticles, and branched submicron channels. Detailed SEM studies about the annealing-induced morphological evolution of our Ag thin films are reported in the mentioned work. An example of this evolution is shown in **Fig. A** in **Appendix A** for the case of the film thickness considered in the present work. In a non-reported study, we carried out preliminary SERS performance studies of these structures. From this study, the microstructure with the best SERS performance was that presenting branched submicron channels. As shown in reference [33] (see **Appendix A**), the completely dewetted samples with isolated micro and nanoparticles have the main disadvantage of presenting a wide distribution of particle sizes, which was manifested in a very anisotropic SERS signal when testing different sample zones. Thus, the branched submicron channels-based structure was selected to carry out more detailed and exhaustive studies as those presented in this work.
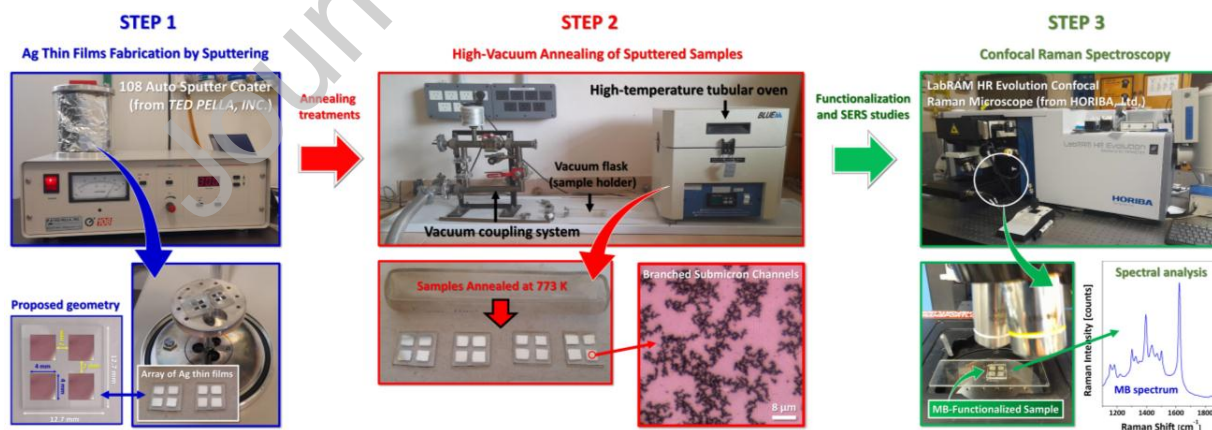

Fig. 1. Schematization of the main experimental steps carried out in this research: Design of the ideal samples' geometry and fabrication of Ag thin films arrays by DC magnetron sputtering (**STEP 1**), high-vacuum annealing of sputtered samples to induce the growth of the desired nanostructure (**STEP 2**) and SERS-based molecular sensing efficiency studies of MB-functionalized samples by confocal Raman spectroscopy (**STEP 3**).

2.3. Samples functionalization. The effects of Ag intrinsic aging (oxidative stress and/or air contamination) on the short-term SERS performance of our samples were especially studied. For this

purpose, one different sample was left in ambient conditions during 1, 2, 3, or 4 weeks after its fabrication. A 50 [µM]-MB ethanolic solution was used as a Raman marker to functionalize the samples

and assess their performance for SERS-based molecular sensing. Thiol groups (SH-) composing this organic dye promote good chemical affinity and stability with noble metals like Au and Ag, making it an ideal analyte for studying their SERS performance [24]. After the corresponding aging period of each sample, 2 [μL] of this solution were dropped on each aged Ag film (4 [mm] x 4 [mm]) and then dried at ambient conditions. Raman spectroscopy studies were immediately carried out after each sample functionalization. An MB surface mass density of approx. 2 [ng/mm2] was estimated for each film surface, considering an MB molar mass of $m_M = 319.85$ [g/mol] [34] and assuming a homogeneous distribution of the MB solution (13 [ng/μL]).

2.4. Raman spectroscopy. A LabRAM HR Evolution Confocal Raman Microscope (from HORIBA, Ltd.) was used for micro-Raman spectroscopy measurements. A DuoScan[TM] module was used to minimize external vibrations in the sample holder stage and ensure the stability of the laser spot position during the spectra acquisition. The Raman spectra were measured at different points of the sample surface using the punctual acquisition mode with a red laser ($\lambda = 633$ [nm]) and a 100X microscope objective. This objective allows us to achieve a laser spot size of ~ 2 [μm] and a maximum output power of 4 [mW]. All measurements were carried out using a laser power of 0.2 [mW] (5 % of the maximum output power). A Raman shift range of 1100 – 2000 [cm^{-1}], a 600 [gr/mm] grid, an acquisition time of 3 [s], and a total of 20 accumulations were the parameters chosen for each spectrum measurement, except when it states otherwise. A monocrystalline Si substrate was used for the Raman shift calibration process, achieving a total of about 5000 counts for 25 % of laser power.

3. Results and discussion

The samples' surface was studied using the optical microscope incorporated with the LabRAM HR Evolution setup to assess their structural homogeneity. **Fig. 2** shows the main microstructural features of the as-deposited and annealed Ag thin films. The optical microscopy resolution does not enable us to observe the as-deposited film microstructure (see **Fig. 2(a)**), but it suggests a homogeneous surface with a compact microstructure. This feature was confirmed by SEM studies, revealing the homogeneous nanocrystalline nature of the as-deposited samples characterized by a compact nanostructure of faceted-like nanocrystals with sizes below 50 [nm] (**Fig. 2(a-1)**).
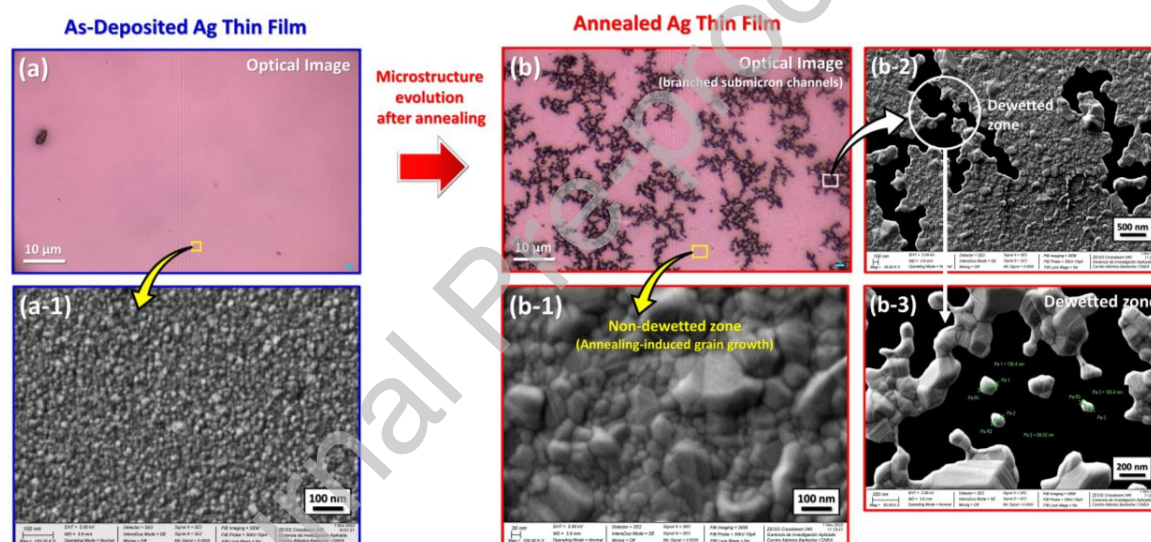

Fig. 2. Optical micrographs of **(a)** as-deposited and **(b)** annealed Ag thin film samples. These images were captured using the LabRAM HR Evolution optical microscope. Additionally, different SEM images with higher magnifications are shown for the case of **(a-1)** an as-deposited film and **(b-1, b-2, b-3)** different characteristic zones of the annealed film. In **Figs. (b)**, **(b-2)** and **(b-3)**, the clear and black zones correspond to the Ag presence and uncovered substrate surface due to dewetting effects, respectively.

For annealed films (see **Fig. 2(b)**), optical microscopy shows the characteristic microstructure expected for the proposed annealing conditions following the reference **[33]**, i.e., samples with the coexistence of partial areas of continuous Ag film surface with grains size growth (**Fig. 2(b-1)**) and complex disordered arrays of branched submicron channels characterized by dewetted zones (**Figs. 2(b-2)** and **(b-3)**). This phenomenon is possible by thermal-induced film dewetting in annealing regimes comparable to the metal melting point ($\sim$ 1235 K for bulk Ag), which can lead to partial dewetting as seen in our case. Dewetting can occur at a solid-liquid, solid-solid **[35]**, or liquid-liquid interface. It describes the retraction process of a fluid forced to cover a non-wettable surface. At room temperature conditions, most thin metal films tend to present quasi-perfect spreading on different kinds of substrates for thickness higher than a critical value (t_c), which can be from units to tens of

nanometers **[36]**. In this situation, the energetically favorable condition at room temperature is usually the growth of a uniform metallic film that covers all the substrate. However, the system can be thermally excited to favor the metal thermal expansion towards the solid-liquid transition (melting point) and lead it to new equilibrium states where the system energy is minimized (thermally-induced dewetting). This fact is crucial to fabricate nanostructures with determined sizes and interesting morphologies for different applications, as previously shown **[33]**. **Fig. 2(b)** clearly shows the partial nature of the thermal-induced dewetting in the Ag thin film. On one hand, typical thermal-induced grain size growth was observed in zones where the Ag thin film conserves its structural integrity (see **Fig. 2(b-1)**). On the other hand, the branched submicron channels exhibit different sub-structures characterized by local zones with the formation of nanometric constrictions/cavities

3

(incomplete or partial dewetting) or isolated nanoparticles (complete dewetting), as shown by **Figs. 2(b-2)** and **(b-3)**, respectively. The combination of these nanostructures could be interesting to promote the electric-near field enhancement of light and the amplification of the SERS signal **[7 – 15]**. Note that these nanostructures were achieved for high-vacuum conditions, and they may not be reproducible for similar annealing temperatures at ambient pressure conditions. Considerable variations in the film surface free energy due to pressure changes could critically affect the dewetting behavior.

As-deposited Ag thin films can be excellent SERS substrates due to the natural emergence of nanostructures associated with the dynamic growth of the deposition process. Typically, thin metallic film surfaces can present nanometric roughness that can result in high electric-near field enhancements due to nanocavities or sharp edges-induced amplification **[37 – 41]**. This phenomenon can favor the emergence of plasmonic hot spots induced by surface topography. Thus, Raman studies on MB-functionalized as-deposited samples would be necessary for assessing the advantages of using the proposed branched submicron channels-based structure for SERS-based molecular sensing. Nevertheless, before any Raman study in functionalized samples, it is necessary to be sure that the detected Raman signal comes from the Raman marker deposited on the sample surface. In this sense, Raman measurements were carried out on both as-deposited and annealed samples without functionalizing. The results are shown in **Appendix B**. In this case, broad Raman peaks associated with symmetric and anti-symmetric stretching vibrations were observed at 1347 [cm^{-1}] and 1578 [cm^{-1}], which could be attributed to carboxylic groups adsorbed on the sample surface **[43 – 44]**. These vibrations could also be associated with Ag oxides, carbon contamination, or the formation of Ag-O-C complexes **[42 – 44]**. As expected, no MB peaks were detected in the Raman spectra.

Fig. 3(a) shows the Raman response of a functionalized as-deposited Ag thin film measured using the acquisition parameters stated in section 2.4. This figure shows different Raman spectra measured in random sample zones. A reproducible SERS signal was generally observed, achieving a reasonably good spectral resolution. The variations between each spectrum were mainly associated with differences in the background baseline signal. This fact could be associated with the heterogeneous grain boundaries that induce an anisotropic light scattering. However, the peak intensities and relative relationship between them are practically the same. For a representative analysis of the Raman peaks, we used the average spectrum shown in **Fig. 3(b)**. Some characteristic peaks associated with the main vibration modes of MB can be observed from this spectrum, being in good agreement with previous reports **[45 – 49]**. The spectrum shows that the characteristic background signals from the as-deposited Ag thin film (see **Fig. B** in **Appendix B**) are not detected and do not affect the spectral resolution of the Raman marker footprint. The most intense peak observed at 1622 [cm^{-1}] can be associated with the main vibration band of MB, which is related to the C-C ring stretching **[46, 47]**. Other main peaks like those observed at 1297 [cm^{-1}] and 1395 [cm^{-1}] can be associated, respectively, with the characteristic in-plane ring deformation of C-H bonds and the symmetrical stretching of C-N bonds in the MB molecular structure **[31, 49]**. These three characteristic peaks are highlighted in **Fig. 3(b)**.

After carrying out the mentioned studies, non-dewetted and branched zones of the annealed samples were studied. As stated in section 2.3, each one of the four samples was functionalized when a certain time passed after its fabrication (1, 2, 3, and 4 weeks).

Immediately after each functionalization instance, the corresponding sample was analyzed by Raman spectroscopy. 5 measurements were carried out in randomly chosen branched zones for each one of the four Ag square films in the 2 x 2 array present in each sample, collecting a total of 20 measurements. This quantity of measurements was chosen to have a statistical representation of the Raman response of this characteristic microstructure. In general, Raman measurements carried out during each test instance (1, 2, 3, or 4 weeks) seem to present a considerable dispersion. Further details on this aspect and the obtained experimental data (individual Raman raw spectra and their relative dispersion) are shown in **Fig. C(a)** of **Appendix C**. This dispersion could be mainly associated with variations in the overall background baseline, coming from the convolution of anisotropic light scattering from heterogeneous interfaces between crystallites that composed the material nanostructure, rather than the intensity of the signal coming from the analyte itself. This fact is exemplified by **Fig. C(b)** shown in **Appendix C**, which shows the Raman spectra observed in the branched zones at the beginning of the test period (after 1 week of aging) normalized by the highest peak at 1623 cm^{-1}. This analysis shows that the Raman spectra are very similar in terms of peak resolution, intensity, relative relationship, and signal/noise ratios, providing the same spectral information in any case from an analytical point of view.
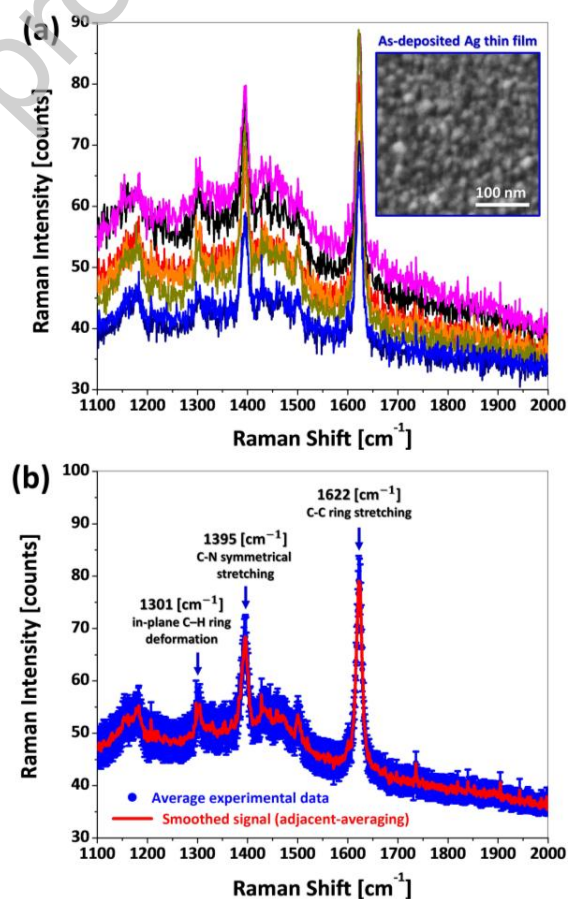

Fig. 3. (a) Different Raman spectra measured in random zones of a functionalized as-deposited Ag thin film. A total of 9 measurements are shown. Each one was acquired using the conditions stated in section 2.4. **(b)** Averaged Raman spectrum (red line) considering those 9 spectra above mentioned. The error bars (blue data) are associated with the experimental standard deviation.

Fig. 4 compares the arithmetical average of 20 Raman spectra acquired for branched and non-dewetted zones in an annealed Ag sample after 1 week of aging. The previously shown results for the as-deposited Ag thin film (data from **Fig. 3(b)**) are also included in this comparison to highlight the advantages of using the branched zones for SERS-based molecular sensing. As expected, a very similar Raman response was observed in the functionalized as-deposited Ag samples concerning that one obtained in functionalized non-dewetted annealed samples, where the Ag thin film conserves its structural continuity. Within the branched submicron channels, equivalent peaks were obtained in random zones but with a considerable amplification of the Raman intensity, leading to higher signal/noise ratios and improved resolution of the characteristic peaks. Different criteria to quantify this amplification can be found in the literature through the well-known "enhancement" factor **[50, 51]**. Nevertheless, an absolute definition is still under discussion.
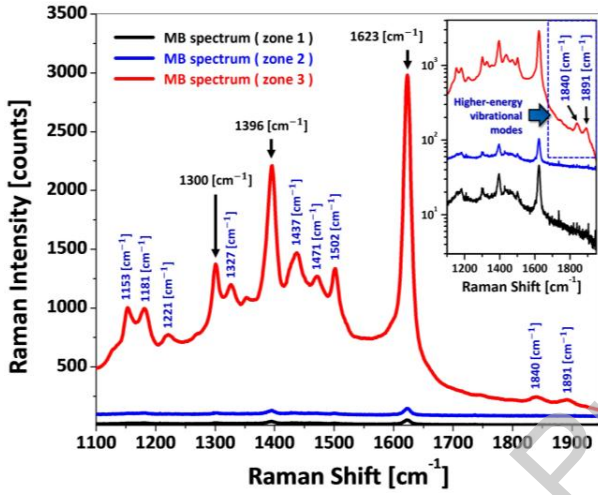

Fig. 4. Comparison between the MB Raman spectra observed for an as-deposited Ag thin film (zone 1, black curve, data extracted from **Fig. 3(b)**), non-dewetted zones (zone2, blue curve), and branched zones (zone 3, red curve). Zone 2 and 3 correspond to an annealed sample with 1 week of aging. The Raman spectra for these zones correspond to an arithmetical average of 20 measurements. Any distinguishable peak from the intrinsic experimental noise has been highlighted. The inset graph shows the same spectra in *log* scale to highlight the differences in the band resolution.

To evaluate the effects of our samples on the SERS signal amplification, we have established a simple criterion to quantify the relative SERS Enhancement Factor (EF_{SERS}) from the experimental Raman Intensity (I) measured at determined Raman shift ($\Delta\tilde{v}$) achieved for branched samples concerning the as-deposited one. Thus, EF_{SERS} is defined as the amplification factor of the absolute Raman intensity observed for branched zones I_b concerning that observed for the as-deposited sample I_a, such that $EF_{SERS} > 1$:

$$EF_{SERS} = \frac{I_b}{I_a} = \frac{I_b(\Delta\tilde{v}_{max}) - I_b(\Delta\tilde{v}_{ref})}{I_a(\Delta\tilde{v}_{max}) - I_a(\Delta\tilde{v}_{ref})} \qquad (1)$$

where $I_b(\Delta\tilde{v}_{max})$ and $I_a(\Delta\tilde{v}_{max})$ correspond to the Raman intensity measured for the most intense peak at $\Delta\tilde{v}_{max} = 1623$ [cm⁻¹] for the branched and as-deposited samples, respectively. $I_b(\Delta\tilde{v}_{ref})$ and $I_a(\Delta\tilde{v}_{ref})$ correspond to the Raman intensity measured at an arbitrarily-chosen reference position $\Delta\tilde{v}_{ref} = 1550$ [cm⁻¹] (the "baseline" intensity) for the branched and as-deposited samples,

respectively. Comparing the absolute intensities measured for the branched zone (zone 3, red curve in **Fig. 4**) $I_b = 2200$ [counts] and the as-deposited one (zone 1, black curve in **Fig. 4**) $I_a = 33$ [counts] using the mentioned criterion, we have calculated an average $EF_{SERS} = 67$. Thus, using branched zones as sensing structures enables to amplify by a factor x67 the analyte Raman signal concerning results achieved for as-deposited samples. This enhanced SERS amplification can be attributed to the complex nanostructures observed within the branched channels' internal matrix (see **Fig. 2(b-2)** and **Fig. 2(b-3)**) that act as plasmonic hot spots **[37 − 41]**, as previously discussed. Unlike the typical Raman signal observed in as-deposited Ag thin films or non-dewetted zones, those achieved in the branched zones enable a more specific chemical "footprint" sensing of the target analyte.

The calculated EF_{SERS} should be considered as a demonstrative parameter since here we are not considering the weight of critical factors like the number of SERS-active nanostructures per unit area (μ_M), the surface density of the molecules adsorbed on the metal (μ_{mol}), the metallic surface area of an individual nanostructure (A_M) and the effective area of the confocal scattering volume of the probing laser (A_{eff}) **[51]**, which are considered in more accurate EF_{SERS} definitions like:

$$EF_{SERS} = \frac{I_{SERS}}{I_{NR}}\left(\frac{N_{NR}}{N_{SERS}}\right) = \frac{I_{SERS}}{I_{NR}}\left(\frac{N_{NR}}{\mu_M \cdot \mu_{mol} \cdot A_M \cdot A_{eff}}\right) , \qquad (2)$$

where I_{SERS} and I_{NR} are the signal intensities measured in SERS and Normal Raman (NR), respectively. Normal Raman signal corresponds to that associated with the as-deposited sample in our case. N_{SERS} and N_{NR} represent the number of probed molecules contributing to SERS and normal Raman signals, respectively. These factors modulate the contribution of the μ_M, μ_{mol}, A_M and A_{eff} parameters in each case to the effective EF_{SERS} value. Considering that μ_M and A_{eff} are much lower for branched zones than as-deposited sample for a constant laser spot size, we could expect $N_{NR}/N_{SERS} \gg 1$ and consequently a much higher EF_{SERS} value to that estimated by using **Eq. (1)**. The highly-anisotropic nature of the morphology distribution of the branched channels makes difficult to analytically determine these factors and give an accurate value for EF_{SERS}. Nevertheless, we can estimate a more accurate value for EF_{SERS} considering the Surface Mass Density $\rho_{SM} = 200$ [ng/cm²] (or 2 x 10⁻⁶ [ng/μm²]) calculated in section 2.3 and the effective metallic area A_{EM} covered by the active sensing area $A_S \cong 4$ [μm²] determined by the laser spot size (see **Appendix C**). **Fig. B** in **Appendix B** shows that the typical proportion of metallic surface coverage in branched submicron channels zones concerning A_S is about of 50 %, such that $A_{EM} \cong 2$ [μm²]. Thus, we can estimate the number of probed molecules within the active sensing area contributing to SERS as:

$$N_{SERS} = \frac{\rho_{SM} N_A A_{EM}}{m_M} \sim 10^6 , \qquad (3)$$

where $m_M = 320$ [g/mol] for MB and $N_A \cong 6$ x 10²³ [molecules/mol] is the Avogadro number. Now, considering the typically reported values for N_{NR} (10¹⁰ − 10¹²) using analytes with concentrations from [mM] to [μM] and similar laser configurations **[19, 20, 22, 23, 52 − 54]**, we estimate the most pessimistic SERS enhancement factor for our samples as:

$$EF_{SERS} = \frac{I_{SERS}}{I_{NR}}\left(\frac{N_{NR}}{N_{SERS}}\right) = \frac{I_b}{I_a}\left(\frac{10^{10}}{10^6}\right) \cong 6.7 \text{ x } 10^5, \qquad (4)$$

which is competitive considering the typical values ($10^4 - 10^8$) reported in the literature for different kinds of Ag nanostructures [19, 20, 22, 23, 52 – 54]. For simplicity, we chose $I_{SERS}/I_{NR} = I_b/I_a$ to do calculations but really $I_{SERS}/I_{NR} \gg I_b/I_a$, since I_a includes considerable intrinsic enhancement contributions from the as-deposited sample. Thus, EF_{SERS} could be considerably higher.

SERS in submicron branched zones additionally enables the identification of lower-energy vibrational modes compared to SERS in non-dewetted zones such as those observed between 1150 and 1250 [cm^{-1}] (see **Fig. 4**), which are typically identified by high-sensitivity SERS-based molecular sensors [31, 55, 56]. In this range, two main peaks were observed at 1153 and 1181 [cm^{-1}], which are commonly associated with the in-plane bending of C-H bonds and stretching of C-N bonds or higher-energy modes associated with C-H in-plane bending [31, 49, 55]. Another peak at 1221 [cm^{-1}] was observed and attributed to the MB chemical footprint in good agreement with previous studies that have observed it [31, 55, 56] but have not been able to clarify the chemical nature of this vibrational state. Other modes at 1327, 1437, 1471, and 1502 [cm^{-1}] are observable from the Raman spectra (compared to SERS in non-dewetted zones), which can be associated with the in-plane ring deformation of C-H (1327 [cm^{-1}]), asymmetrical stretching of C-N bonds (1437 and 1471 [cm^{-1}]) and asymmetrical stretching of C-C bonds [31, 49, 55].

We have also identified other higher-energy vibrational modes (1840 and 1891 [cm^{-1}], as shown by the inset graph in **Fig. 4**) concerning the highest-intensity mode for MB (1623 [cm^{-1}]), which have not been reported in other similar studies. Experimental evidence found in the literature suggests that the origin of these peaks cannot come from vibrational modes of other species inherently present in the samples such as Si (substrate) [57] or ethanol (solvent used for MB dissolution) [58 – 60]. Thus, those peaks could be associated with some MB vibrational modes, which is also supported by a previous analysis (see **Fig. B** in **Appendix B**) that evidences no peaks between 1700 and 2000 [cm^{-1}] in non-functionalized samples. These characteristics are attractive and desired in efficient SERS substrates to ensure a better chemical specificity and spectral resolution for the correct discrimination between two or more molecules with similar vibrational responses. Moreover, this kind of nanostructure not only enables to identify more vibrational states but also promotes exceptionally higher signal/noise ratios.

In general, the scientific community agrees that competitive sensitivity usually ranges in the order of $10^0 - 10^2$ [ng/cm^2] [61 – 71]. On the other hand, considerably lower sensitivities have been reported in a few situations, achieving magnitudes about $10^{-2} - 10^{-1}$ [ng/cm^2] [63, 67] or even lower, about 10^{-3} [ng/cm^2] [69]. In this study, exceptional spectral resolution has been observed for a relatively low surface mass density of MB, which is about 2 [ng/mm^2] or equivalently 200 [ng/cm^2]. Indeed, the exceptionally good spectral resolution observed for the surface mass density used in our case enables us to speculate on achieving even higher SERS signals for lower surface mass densities. Thus, these results demonstrate that the proposed branched submicron channels in annealed ultra-thin Ag films are an advantageous alternative for high-resolution and competitive-sensitivity SERS-based molecular sensing.

Fig. 5(a) shows the average Raman spectra measured in branches zones on each functionalization instance carried out for substrate aging studies. A total of 20 measurements were considered per average spectrum. The raw data associated with these measurements can be seen in more detail in **Fig. C(a)** of **Appendix C**. Results show that the substrate aging effects on the Raman signal seem to be negligible for the considered period, which evidences the exceptional short-term lifespan stability of our samples for SERS-based molecular sensing applications. This fact suggests that the inherent formation of Ag native oxides or the adsorption of carbon-based contaminants on the sample surface over time does not negatively affect the plasmonic behavior of the structures responsible for the Raman signal enhancement. A small decrease in the Raman signal intensity seems to occur between the first two weeks of aging, observing a more significant decrease for three and four weeks. This variation could be also associated with the observed variations in the overall background signal, as previously discussed. On the other hand, the background and absolute averaged intensity of the Raman signal seem to stabilize at similar values between three and four weeks. While the results suggest that the substrate aging in the short term negatively affects the Raman signal amplification, this does not significantly impact on the spectral resolution and definition of the analyte chemical footprint.

To quantitively demonstrate the substrate aging impact, we calculated the absolute intensity of the three main Raman peaks observed for each aging period. The considered peaks are shown in **Fig. 5(b)** and correspond to those highlighted as peak 1, 2, and 3 in **Fig. 5(a)**. The absolute intensity $I_b^{i,j}$ of the i-th peak for the j-th week was calculated following the same logic stated by **Eq. (1)**:

$$I_b^{i,j} = I_b^{i,j}(\Delta\tilde{\nu}_{max}) - I_b^{i,j}(\Delta\tilde{\nu}_{ref}), \tag{5}$$

where $(\Delta\tilde{\nu}_{max}, \Delta\tilde{\nu}_{ref}) =$ (1623 [cm^{-1}], 1550 [cm^{-1}]), $(\Delta\tilde{\nu}_{max}, \Delta\tilde{\nu}_{ref}) =$ (1396 [cm^{-1}], 1360 [cm^{-1}]) and $(\Delta\tilde{\nu}_{max}, \Delta\tilde{\nu}_{ref}) =$ (1300 [cm^{-1}], 1280 [cm^{-1}]) for $I_b^{1,j}$, $I_b^{2,j}$ and $I_b^{3,j}$, respectively. Thus, the values of the absolute intensities for each peak and their evolution concerning the substrate aging are shown in **Fig. (c)**. These results evidence the previous observations, showing the generalized decrease of the peaks' Raman intensity for longer aging periods and the saturation of the intensity decay. This intensity stabilization could be a promising feature for achieving a SERS performance with short-term stability and reproducibility, especially when considering SERS substrates that require considerable storage and/or transport periods before functionalization and Raman measurements.

Using the calculated absolute Raman intensities above mentioned for each peak and substrate aging period, we also calculated the EF_{SERS} parameter to assess the aging effects. Analogously to **Eq. (1)**, we calculated $I_a^i(\Delta\tilde{\nu}_{max}) - I_a^i(\Delta\tilde{\nu}_{ref}) = 33$, 18 and 8 [counts] for the i-th peaks 1, 2 and 3 observed in the as-deposited sample, respectively. These values were used for calculating the $EF_{SERS} = I_b^{i,j}/I_a^i$, obtaining the results shown in **Fig. 5(d)**. Note that the EF_{SERS} magnitude seems to be relatively constant for any peak, within a reasonable error margin, since this factor is normalized by the absolute intensity of each peak of the reference sample (the as-deposited film). This fact suggests that the Raman intensity of any peak measured in the branched zones is amplified in the same proportion, indicating that these zones do not favor the excitation of preferential vibrational states. Moreover, **Fig. 5(d)** shows that the enhancement factor is negatively affected by substrate aging, which is consistent with the tendency observed in **Fig. 5(c)**.
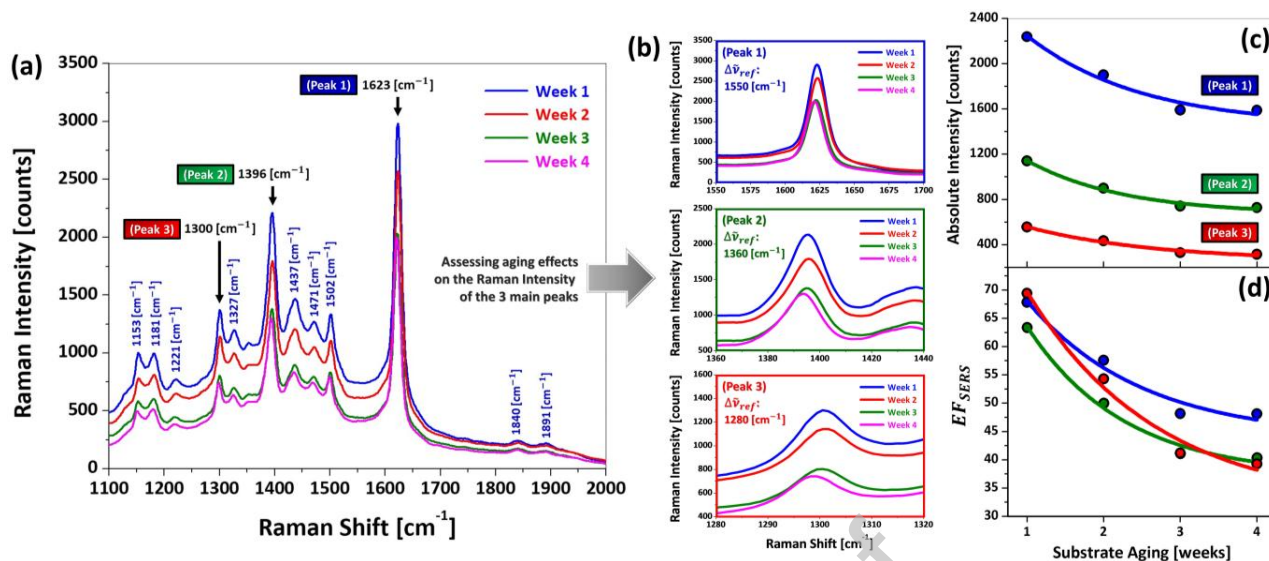
Fig. 5. (a) Average Raman spectra measured in branched zones on each functionalization instance (1, 2, 3, and 4 weeks) carried out for substrate aging studies. A total of 20 measurements were considered per average spectrum. The three main peaks of MB at 1623, 1396, and 1300 [cm^{-1}] are highlighted as peaks 1, 2 and 3, respectively. **(b)** Magnification of each one of these peaks, which were used for calculating the absolute Raman intensity and assessing the impact of the substrate aging on its evolution. The evolution of the **(c)** absolute Raman intensity and **(d)** enhancement factor EF_{SERS} for each one of the three main peaks concerning the substrate aging period are shown.

In addition to the perspectives for competitive-sensitivity SERS, the studied samples have also shown potential for fast SERS analysis. Fast sensing involves measurement times between a few seconds and one minute while maintaining high spectral resolution **[61, 63, 64, 66, 68, 69, 70 – 73]**. While the previous Raman spectra were measured with a total acquisition time of 1 minute (20 accumulations and 3 [s] of acquisition per each one), a similar spectral resolution can be achieved even reducing the measurement time. **Fig. 6** shows Raman spectra measured using different total acquisition times from 0.05 to 10 [s] with one accumulation. The other measurement conditions were set equal to those mentioned in Section 2.4. Results demonstrate that good signal enhancement is achieved even reducing the total acquisition times to values as low as 0.5 [s]. An acceptable spectral resolution is achieved for shorter times (0.1 – 0.05 [s]) but with a significant increment in the signal/noise ratio.

Using fast spectroscopy, low laser beam powers, and short exposure times for analytes is particularly important for sensing organic and biological molecules, which can be chemically deteriorated under excessive laser power (over 1 [mW]) **[74 – 76]**. In this context, a low operation power of 0.2 [mW] was chosen for our studies. Additionally, the measurement time was considerable minimized while achieving high spectral resolution to ensure good SERS performance of our samples under short exposure conditions, making them ideal for detection of highly photosensitive molecules.

The relevance of the branched zones as Raman signal hot spots was demonstrated by fast μ-Raman mapping measurements in a functionalized annealed sample. This study was carried out in the sample with 1 week of aging, and it is useful to find correlations between the microstructure and spatial distribution of the hot spots. **Fig. 7** shows the measured Raman intensity map, which evidences a clear correlation between the spatial distribution of the sample microstructural features (branched channels) and Raman intensity hot spots. These hot spots are generally observed in the branched channels and represent the sample zones where the SERS

signal achieves the best enhancement. This fact is consistent with previous results from punctual acquisition-Raman studies that show the exceptional Raman signal enhancement of these zones.
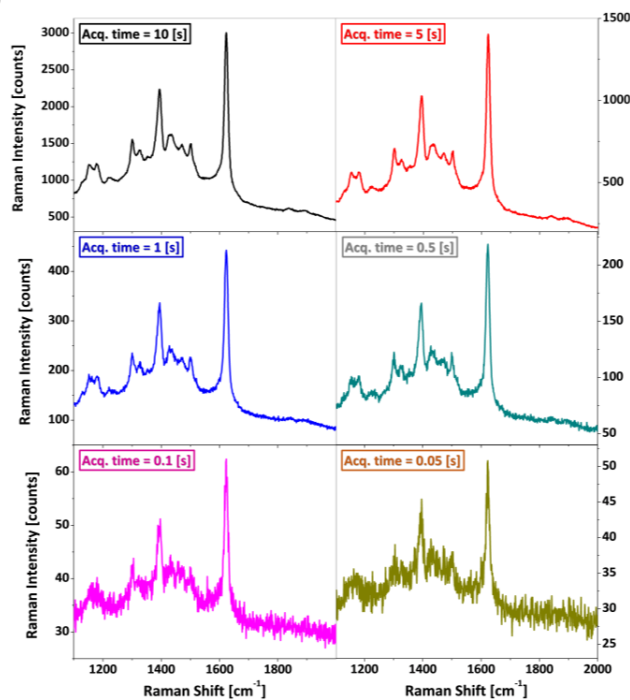

Fig. 6. Raman spectra measured in branched zones of the last tested sample (week 4) using different acquisition times from 0.05 to 10 [s] with one accumulation. The other measurement conditions (laser power, grid, microscope objective, etc.) were set equal to those mentioned in Section 2.4.

Raman mapping studies demonstrate the exceptional efficiency of these nanostructures for fast and good-sensitivity molecular

detection. Quantitatively, an MB surface density of 2 [ng/mm^2] on the whole sample surface was estimated assuming the theoretical MB density and the amount of MB deposited on it, as explained in Section 2.3. Considering a 0.25 [µm^2]-testing area for each pixel of µ-Raman mapping of **Fig. 7**, where the measured spectra for the branched channels are typically like those observed for green and yellow pixels, we can estimate a mass-sensing sensitivity in the order of 1 x 10^{-15} [g/µm^2] that can be detected with high spectral resolution.

While the gross potential of branched Ag samples for efficient SERS-based molecular sensing has been demonstrated, other relevant studies could be interesting to carry out in the future to assess their whole potential. For example, systematic Raman studies on samples with lower MB concentrations would enable us to define the sensitivity limits of this kind of samples. On the other hand, it could be interesting to study the effects of the analyte bleaching on the time stability of the Raman response (by light and/or air exposition) and the signal stabilization over longer periods, which is critical when functionalized substrates require considerable storage and/or transport time before Raman measurements. Thus, this work opens new paradigms and perspectives for future studies that could disclose more interesting features about these samples for SERS-based molecular sensing.
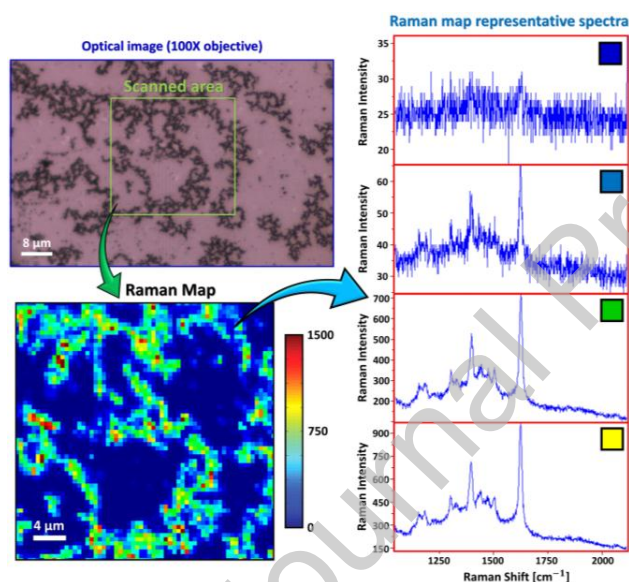

Fig. 7. µ-Raman mapping studies with submicron spatial resolution carried out in an annealed Ag thin film sample functionalized after 1 week of aging. A pixel size of 500 [nm], acquisition time (per pixel) = 1 [s], and accumulation (per pixel) = 2 were the set parameters. The other parameters were the same as stated in Section 2.4. The upper left image shows an optical view of the scanned area, and the lower left one shows the measured Raman intensity map associated with that area. The intensity color scale was set considering the most intense peak at 1623 [cm-1] observed for the MB Raman spectrum as a reference. The Raman spectra panel shown on the right side highlights some typical spectra associated with representative pixel colors.

4. Conclusions

Efficient SERS substrates based on thermally-induced branched submicron channels in ultra-thin Ag films have been successfully fabricated. Thermal-induced dewetting mechanisms at determined annealing conditions have enabled us to fabricate a complex matrix of branched submicron channels in Ag thin films. This microstructure

can be used as an efficient local amplifier (hot spots) for the analyte Raman signal, as demonstrated by systematic confocal Raman spectroscopy studies. Exceptional Raman spectral resolution can be achieved by using these structures, which was evidenced by high enough signal/noise ratios to identify the analyte main vibrational modes and its characteristic chemical footprint. The fabricated samples have demonstrated the potential for fast SERS determinations, observing good spectral resolution quality even by reducing the measurement time from 1 minute up to less than 1 [s]. Substrate aging effects on the degradation of the SERS performance show a small decrease in the SERS intensity after the first week of aging, observing a systematic decrease for longer aging periods but keeping high enough intensity values compared to the initial ones and similar band resolution and relative peaks aspect ratios over the considered aging period. This fact evidences a relatively good short-term stability of our samples' lifespan for SERS-based molecular sensing. This fact suggests that the inherent formation of Ag native oxides or the adsorption of carbon-based contaminants on the sample surface over time is a factor that does not negatively affect the SERS signal enhancement after the first week of aging and does not change the molecule spectral bands. In general, high-resolution Raman spectral acquisition for a surface mass density of 2 [ng/mm^2], short measurement times from 0.5 to 60 [s], and highly reproducible SERS performance in the short term are the main features of our samples. These results show the proposed structures are promising candidates for designing high-sensitivity, fast, and time-stable SERS substrates, representing a simple and low-cost alternative for efficient SERS-based molecular (bio)sensing.

Data availability statement

The datasets generated and analyzed during the current study are available from the corresponding authors on reasonable request.

Declaration of competing interest

The authors declare that they have no known competing financial interests or personal relationships that could have influenced the work reported in this paper.

Acknowledgements

References

[1] S. Kasani, K. Curtin, N. Wu, Nanophotonics 8 **(2019)** 2065-2089, https://doi.org/10.1515/nanoph-2019-0158
[2] B. Dietzek, D. Cialla, M. Schmitt, J. Popp, Introduction to the Fundamentals of Raman Spectroscopy, Confocal Raman Microscopy. Springer Series in Surface Sciences, Vol. 66. Springer, Cham, **2018**, pp. 47 - 68, https://doi.org/10.1007/978-3-319-75380-5_3

[3] P. Mandal, B. S. Tewari, Surfaces and Interfaces 28 **(2022)** 101655, https://doi.org/10.1016/j.surfin.2021.101655

[4] K. Xu, R. Zhou, K. Takei, M. Hong, Advanced Science 6 **(2019)** 1900925, https://doi.org/10.1002/advs.201900925

[5] R. Shi, X. Liu, Y. Ying, Journal of Agricultural and Food Chemistry 66 **(2018)** 6525-6543, https://doi.org/10.1021/acs.jafc.7b03075

[6] U. Aslam, S. Chavez, S. Linic, Nature Nanotechnology 12 **(2017)** 1000-1005, https://doi.org/10.1038/nnano.2017.131

[7] Haitao Hu, Xue Lu, Kai Chen, Zhendong Yan, Pinggen Cai, Chaojun Tang, Optics Communications 502 **(2022)** 127441, https://doi.org/10.1016/j.optcom.2021.127441

[8] Meitong Nie, Yuming Zhao, Wonil Nam, Junyeob Song, Wenqi Zhu, H. J. Lezec, A. Agrawal, Wei Zhou, Advanced Functional Materials 32 **(2022)** 220231, https://doi.org/10.1002/adfm.202202231

[9] Wei Zhang, Tianxing Zheng, Bin Ai, Panpan Gu, Yuduo Guan, Yu Wang, Zhiyuan Zhao, Gang Zhang, Applied Surface Science 593 **(2022)** 153388, https://doi.org/10.1016/j.apsusc.2022.153388

[10] R. Chikkaraddy, A. Xomalis, L. A. Jakob, J. J. Baumberg, Light: Science & Applications 11 **(2022)** 1-9, https://doi.org/10.1038/s41377-022-00709-8

[11] Le Liang, Peng Zheng, Chi Zhang, I. Barman, Advanced Materials 33 **(2021)** 2005133, https://doi.org/10.1002/adma.202005133

[12] A. Xomalis, Xuezhi Zheng, A. Demetriadou, A. Martínez, R. Chikkaraddy, J. J. Baumberg, Nano Letters 21 **(2021)** 2512-2518, https://doi.org/10.1021/acs.nanolett.0c04987

[13] G. Palermo, M. Rippa, Y.Conti, A. Vestri, R. Castagna, G. Fusco, E. Suffredini, Jun Zhou, J. Zyss, A. De Luca, L. Petti, Applied Materials & Interfaces 13 **(2021)** 43715-43725, https://doi.org/10.1021/acsami.1c12525

[14] Hongbo Wang, Gaofeng Rao, Yang Wang, Xinchuan Du, Miao Zhang, Xuepeng Wang, Anjun Hu, Yin Hu, Jianwen Huang, Junwei Chu, Xianfu Wang, Linmao Qian, Jie Xiong, The Journal of Physical Chemistry C 125 **(2021)** 4710-4719, https://doi.org/10.1021/acs.jpcc.0c11071

[15] A. Nana Koya, Joao Cunha, Tian-Long Guo, A. Toma, D. Garoli, Tao Wang, S. Juodkazis, Dan Cojoc, R. Proietti Zaccaria, Advanced Optical Materials 8 **(2020)** 1901481, https://doi.org/10.1002/adom.201901481

[16] B. Ankamwar, S. Gharpure, Nano Express 1 **(2020)** 010020, https://doi.org/10.1088/2632-959X/ab85b4

[17] X. Xia Han, R. S. Rodriguez, C. L. Haynes, Y. Ozaki, B. Zhao, Nature Reviews Methods Primers 1 **(2021)** 87, https://doi.org/10.1038/s43586-021-00083-6

[18] C. M. Muntean, D. Cuibus, S. Boca, A. Falamas, N. Tosa, I. A. Brezeştean, A. Bende, L. Bardu-Tudoran, R. Moldovan, E. Bodoki, C. Farcău, Biosensors 13 **(2023)** 530, https://doi.org/10.3390/bios13050530

[19] Ming-Hua Shiao, Tsunghsueh Wu, Hung Ji Huang, Ching-Yi Peng, Yung-Sheng Lin, Ting-Yu Lai, Yang-Wei Lin, Nanomaterials 11 **(2021)** 1359, https://doi.org/10.3390/nano11061359

[20] Taeksu Lee, Soongeun Kwon, Sanghee Jung, Hyungjun Lim, Jae-Jong Lee, Nano Research 12 **(2019)** 2554-2558, https://doi.org/10.1007/s12274-019-2484-7

[21] R. Nisticò, P. Rivolo, Ch. Novara, F. Giorgis, Colloids and Surfaces A: Physicochemical and Engineering Aspects 578 **(2019)** 123600, https://doi.org/10.1016/j.colsurfa.2019.123600

[22] J. Sitjar, Jiunn-Der Liao, Han Lee, Li Peng Pan, B. Haochih Liu, Wei-en Fu, Guo Dung Chen, Nanomaterials 9 **(2019)** 1750, https://doi.org/10.3390/nano9121750

[23] Yiran Tian, Hongmei Liu, Ying Chen, Canliang Zhou, Yong Jiang, Chenjie Gu, Tao Jiang, Jun Zhou, Sensors and Actuators B: Chemical 301 **(2019)** 127142, https://doi.org/10.1016/j.snb.2019.127142

[24] G.-Z. Peng, A. Hardiansyah, H.-T. Lin, R.-Y. Lee, C.-Y. Kuo, Y.-C. Pu, T.-Y. Liu, Surface and Coatings Technology 435 **(2022)** 128212, https://doi.org/10.1016/j.surfcoat.2022.128212

[25] R.-S. Juang, Y.-W. Cheng, W.-T. Chen, K.-S. Wang, C.-C. Fu, S.-H. Liu, R.-J. Jeng, C.-C. Chen, M.-C. Yang, T.-Y. Liu, Applied Surface Science 521 **(2020)** 146372, https://doi.org/10.1016/j.apsusc.2020.146372

[26] Y.-W. Cheng, C.-H. Wu, W.-T. Chen, T.-Y. Liu, R.-J. Jeng, Applied Surface Science 469 **(2019)** 887-895, https://doi.org/10.1016/j.apsusc.2018.11.100

[27] T. Cwalinski, W. Polom, L. Marano, G. Roviello, A. D'Angelo, N. Cwalina, M. Matuszewski, F. Roviello, J. Jaskiewicz, K. Polom, Journal of Clinical Medicine 9 **(2020)** 3538, https://doi.org/10.3390/jcm9113538

[28] I. Khan, K. Saeed, I. Zekker, B. Zhang, A. H. Hendi, A. Ahmad, S. Ahmad, N. Zada, H. Ahmad, L. A. Shah, T. Shah, I. Khan, *Water* 14 **(2022)** 242, https://doi.org/10.3390/w14020242

[29] R. S. Pushparajah Mak, E. L. Liebelt, Pediatric Emergency Care 37 **(2021)** 474-477, https://doi.org/10.1097/PEC.0000000000002526

[30] N. X. Dihn, T. Q. Huy, L. V. Vu, L. T. Tam, A.-T. Le, Journal of Science: Advanced Materials and Devices 1 (2016) 84-89, https://doi.org/10.1016/j.jsamd.2016.04.007

[31] T. Xu, X. Wang, Y. Huang, K. Lai, Y. Fan, Food Control 106 **(2019)** 106720, https://doi.org/10.1016/j.foodcont.2019.106720

[32] Q. D. Mai, H. A. Nguyen, N. X. Dihn, N. T. T. Thuy, Q. H. Tran, P. C. Thanh, A.-T. Pham, A.-T. Le, Talanta 253 **(2023)** 124114, https://doi.org/10.1016/j.talanta.2022.124114

[33] S. Roa, M. J. Cortés Burgos, Materials Letters 336 **(2023)** 133863, https://doi.org/10.1016/j.matlet.2023.133863

[34] A. Fernández-Pérez, T. Valdés-Solís, G. Marbán, Dyes and Pigments **(2019)** 448-456, https://doi.org/10.1016/j.dyepig.2018.09.083

[35] F. Leroy, L. Borowik, F. Cheynis, Y. Almadori, S. Curiotto, M. Trautmann, J. C. Barbé, P. Müller, Surface Science Reports 71 **(2016)** 391-409, https://doi.org/10.1016/j.surfrep.2016.03.002

[36] J. T. Gudmundsson, Plasma Sources Science and Technology 29 **(2020)** 113001, https://doi.org/10.1088/1361-6595/abb7bd

[37] J. V. Perales-Rondon, A. Colina, M. C. González, A. Escarpa, Applied Materials Today 20 **(2020)** 100710, https://doi.org/10.1016/j.apmt.2020.100710

[38] J. Wang, C. Qiu, X. Mu, H. Pang, X. Chen, D. Liu, Talanta 210 **(2020)** 120631, https://doi.org/10.1016/j.talanta.2019.120631

[39] A. El Guerraf, M. Bouabdallaoui, Z. Aouzal, S. Ben Jadi, N. K. Bakirhan, M. Bazzaoui, S.A. Ozkan, E.A. Bazzaoui, Journal of Electroanalytical Chemistry 882 **(2021)** 115034, https://doi.org/10.1016/j.jelechem.2021.115034

[40] J. Wang, L. Ma, X. Ding, S. Wu, X. Guo, D. Zhang, Applied Spectroscopy Reviews **(2022)** 1-24, https://doi.org/10.1080/05704928.2022.2129667

[41] T. Jones, Materials Science and Technology **(2023)** 1-15, https://doi.org/10.1080/02670836.2023.2197729

[42] D. Büchel, C. Mihalcea, T. Fukaya, N. Atoda, J. Tominaga, T. Kikukawa, H. Fuji, Applied Physics Letters 79 **(2001)** 620-622, https://doi.org/10.1063/1.1389513

[43] L. Wang, C. Wan, Y. Fu, H. Chen, X. Liu, M. Li, Journal of Electronic Materials 4 **(2014)** 132-136, https://doi.org/10.1007/s11664-013-2765-y

[44] N. Joshi, N. Jain, A. Pathak, J. Singh, R. Prasad, C. P. Upadhyaya, Journal of Sol-Gel Science and Technology 86 **(2018)** 682-689, https://doi.org/10.1007/s10971-018-4666-2

[45] G. Laurent, N. Félidj, J. Aubard, G. Lévi, J. R. Krenn, A. Hohenau, G. Schider, A. Leitner, F. R. Aussenegg, Physical Review B 71 **(2005)** 045430, https://doi.org/10.1103/PhysRevB.71.045430

[46] M. Jung, S. K. Kim, S. Lee, J. H. Kim, D. H. Woo, Journal of Nanophotonics 7 **(2013)** 073798, https://doi.org/10.1117/1.JNP.7.073798

[47] V. Sans, A. Moskalenko, K. Wilson, V. Kozhevin, D. Yavsin, I. Kuzmin, S. Gurevichde, A. Lapkin, Analyst 136 **(2011)** 3295-3302, https://doi.org/10.1039/C1AN15378A

[48] M. Šubr, M. Procházka, Nanomaterials 8 **(2016)** 418, https://doi.org/10.3390/nano8060418

[49] M. P. Rodríguez-Torres, L. A. Díaz-Torres, S. Romero-Servin, International Journal of Molecular Sciences 15 **(2014)** 19239-19252, https://doi.org/10.3390/ijms151019239

9

[50] E. C. Le Ru, E. Blackie, M. Meyer, P. G. Etchegoin. *The Journal of Physical Chemistry C* 111 **(2007)** 13794-13803. https://doi.org/10.1021/jp0687908

[51] E. Cara, L. Mandrile, A. Sacco, A. M. Giovannozzi, A. M. Rossi, F. Celegato, N. De Leo, P. Hönicke, Y. Kayser, B. Beckhoff, D. Marchi, A. Zoccante, M. Cossi, M. Laus, L. Boarino, F. F. Lupi. *Journal of Materials Chemistry C* 8 **(2020)** 16513-16519. https://doi.org/10.1039/D0TC04364H

[52] Y.-H. You, Y.-W. Lin, C.-Y. Chen. *RSC Advances* 5 **(2015)** 93293. **https://doi.org/10.1039/c5ra18085f**

[53] Y.-W. Lin, C. Tang. *The Journal of Physical Chemistry* C 119 **(2015)** 24865-24874. **https://doi.org/10.1021/acs.jpcc.5b08375**

[54] H. K. Park, J. K. Yoon, K. Kim. *Langmuir* 22 **(2006)** 1626-1629. **https://doi.org/10.1021/la052559o**

[55] C. Li, Y. Huang, K. Lai, B. A. Rasco, Y. Fan, Food Control 65 **(2016)** 99-105, http://dx.doi.org/10.1016/j.foodcont.2016.01.017

[56] J. A. Anastasopoulos, A. S. Beobide, A. C. Manikas, G. A. Voyiatzis, Journal of Raman Spectroscopy 48 **(2017)** 1762-1770, https://doi.org/10.1002/jrs.5233

[57] R. Kumar, M. Tanwar, Journal of Raman Spectroscopy 52 **(2021)** 2100-2118, https://doi.org/10.1002/jrs.6272

[58] A. Picard, I. Daniel, G. Montagnac, P. Oger, Extremophiles 11 **(2007)** 445-452, https://doi.org/10.1007/s00792-006-0054-x

[59] S. O. Konorov, M. W. Blades, R. F. B. Turner, Optics Express 19 **(2011)** 25925-25934, https://doi.org/10.1364/OE.19.025925

[60] A. Khetani, J. Riordon, V. Tiwari, A. Momenpour, M. Godin, H. Anis, Optics Express 21 **(2013)** 12340-12350, https://doi.org/10.1364/OE.21.012340

[61] L. Ouyang, P. Dai, L. Yao, Q. Zhou, H. Tang, L. Zhu, Analyst 144 **(2019)** 5528-5537, https://doi.org/10.1039/C9AN01123D

[62] G. Kwon, J. Kim, D. Kim, Y. Ko, Y. Yamauchi, J. You, Cellulose 26 **(2019)** 4935-4944, https://doi.org/10.1007/s10570-019-02427-8

[63] D. Huang, J. Zhao, M. Wang, S. Zhu, Food Control 108 **(2020)** 106835, https://doi.org/10.1016/j.foodcont.2019.106835

[64] L. Xu, H. Liu, H. Zhou, M. Hong, Talanta 228 **(2021)** 122204, https://doi.org/10.1016/j.talanta.2021.122204

[65] F. Bai, J. Dong, J. Qu, Z. Zhang, Nanotechnology 32 **(2021)** 385501, https://doi.org/10.1088/1361-6528/ac09ab

[66] H. Lu, M. Jin, Z. Zhang, S. Wu, L. Shui, Nanomaterials 12 **(2022)** 1191, https://doi.org/10.3390/nano12071191

[67] F. Meng, A. Aihaiti, X. Li, W. Zhang, Y. Qin, N. Zhu, M. Zhang, Biosensors and Bioelectronics 203 **(2022)** 114031, https://doi.org/10.1016/j.bios.2022.114031

[68] D. Xia, P. Jiang, Z. Cai, R. Zhou, B. Tu, N. Gao, G. Chang, H. He, Y. He, Microchimica Acta 189 **(2022)** 232, https://doi.org/10.1007/s00604-022-05328-z

[69] A. Lorena Picone, M. L. Rizzato, A. R. Lusi, R. M. Romano, Food Chemistry 373 **(2022)** 131570, https://doi.org/10.1016/j.foodchem.2021.131570

[70] M. Chen, J. Zhang, X. Zhu, Z. Liu, J. Huang, X. Jiang, F. Fu, Z. Lin, Y. Dong, ACS Applied Materials and Interfaces 14 **(2022)** 26216-26224, https://doi.org/10.1021/acsami.2c04087

[71] N. Mahar, M. Haroon, T. A. Saleh, A. A. Al-Saadi, Journal of Molecular Liquids 343 **(2021)** 117633, https://doi.org/10.1016/j.molliq.2021.117633

[72] F. Xu, W. Shang, G. Ma, Y. Zhu, M. Wu, Sensors and Actuators B: Chemical 326 **(2021)** 128968, https://doi.org/10.1016/j.snb.2020.128968

[73] F. U. Ciloglu, M. Hora, A. Gundogdu, M. Kahraman, M. Tokmakci, O. Aydin, Analytica Chimica Acta 1221 **(2022)** 340094, https://doi.org/10.1016/j.aca.2022.340094

[74] V. Shvalya, G. Filipič, J. Zavašnik, I. Abdulhalim, U. Cvelbar, Applied Physics Reviews 7 **(2020)** 031307, https://doi.org/10.1063/5.0015246

[75] J. Perumal, Y. Wang, A. B. E. Attia, U. S. Dinish, M. Olivo, Nanoscale 13 **(2021)** 553-580, https://doi.org/10.1039/D0NR06832B

[76] S. Mitra, M. Basak, Materials Today 57 **(2022)** 225-261, https://doi.org/10.1016/j.mattod.2022.05.023

Appendix A: Annealing-induced morphological evolution of the Ag thin film.

A wide variety of Ag-based microstructures like disordered nanoholes, micro and nanoparticles, and branched submicron channels can be fabricated depending on the initial Ag thin film thickness and annealing temperature. This fact was demonstrated in our previous research by SEM and optical imaging studies **[27]**. Modifying both conditions enables us to access different dewetting regimes and hence to different kinds of nanostructures. **Fig. A** shows the particular case of the annealing-induced morphological evolution of a 23 [nm]-thick Ag thin film. For low annealing temperatures (573 K) concerning the Ag melting point (1235 K), we can observe a typical annealing-induced grain growth. In this regime, the film conserves a complete spreading on the substrate surface, i.e., thermal energy is not high enough to activate dewetting mechanisms. As the temperature is increased (773 K), partial dewetting mechanisms are activated producing the emergence of submicron branched channels. Finally, as the temperature increases (993 K) closer to the metal melting point, complete dewetting is achieved and characterized by the distribution of isolated micro and nanoparticles.
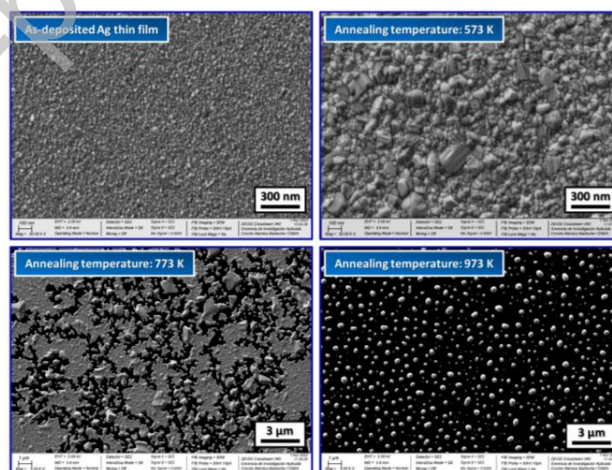

Fig. A. Annealing-induced morphological evolution of a 23 [nm]-thick Ag thin film for temperatures of 573, 773 and 973 K. The annealing time ramp conditions were the same to those stated in section 2.2.

Appendix B: Control measurements on annealed and not annealed Ag samples, without any functionalization.

Before beginning with Raman studies in MB-functionalized samples, it is necessary to bear out the presence of extrinsic spectral signals to this analyte. To assess and identify other external signals in the Raman response of the annealed samples (other than those expected from MB), and to bear them in mind for future analysis, Raman measurements were carried out in MB-unfunctionalized samples (**Fig. B**). **Fig. B(a)** shows the laser spot size used for Raman measurements, which enables to sense the intrinsic Raman response of non-dewetted zones with areas as low as 4 [μm^2]. The diffraction-limited spatial resolution is enough to discriminate between non-

dewetted and branched channel zones. The analyzed zones are characterized by typical thermal-induced grain growth, as shown in the magnification of **Fig. B(a)**.

Characteristic Raman spectra measured for unfunctionalized annealed samples in non-dewetted zones where the Ag thin film conserves its structural continuity are shown in **Fig. B(b)**. As expected, no MB peaks are observed in the Raman spectra. However, two broad peaks can be observed at 1347 [cm^{-1}] and 1578 [cm^{-1}]. Similar characteristics have been observed in other research studies of Ag nanostructures Raman response **[36 − 38]**. While some doubts have arisen concerning the origin of these peaks, it is not clear if they are associated with induced or native Ag oxides, contamination by carbon, or the formation of Ag-O-C complexes. Nevertheless, a general agreement is the hypothesis of a strong influence of carboxylic symmetric (1347 [cm^{-1}]) and anti-symmetric (1578 [cm^{-1}]) C=O stretching vibration of carboxylic groups adsorbed on the sample surface **[36 − 38]**. Thus, the emergence of these peaks in our samples could be associated with external carbon-oxygen contamination. A very similar Raman response to that observed in **Fig. B(b)** was also observed in as-deposited Ag samples (not shown).

Similar peaks can be observed for the Raman response of the branched channels, as shown in **Fig. B(b)**. In this case, random zones within the branched submicron channels were analyzed. The main difference is the considerable amplification of the Raman intensity, which leads to considerably higher signal/noise ratios. This enables to get better resolution of the characteristic peaks. This improved amplification could be due to the complex nanostructures observed within the branched channels internal matrix (see **Fig. 2(b-2)** and **Fig. 2(b-3)**) that could be acting as plasmonic hot spots **[31 − 35]**, as previously discussed.
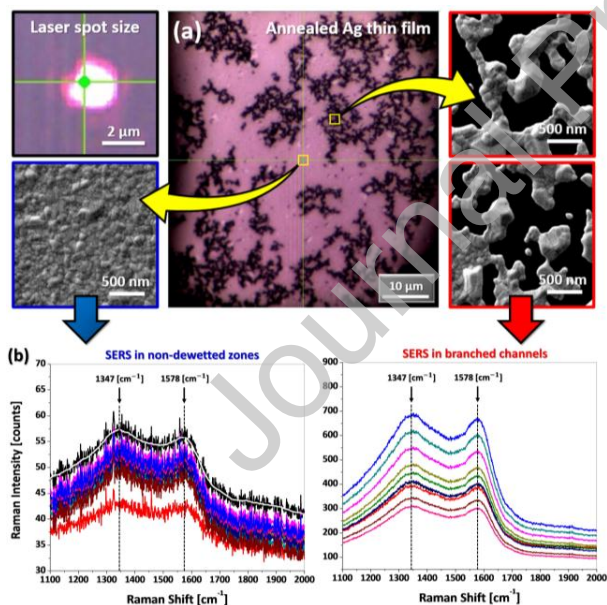

Fig. B. (a) Typical areas of non-dewetted and branched zones in the annealed samples analyzed by Raman spectroscopy. SEM images show the typical nanostructure observed at the Raman measurement scale ($\sim$ 4 [μm^2]) in both cases. The laser spot size ($\sim$ 2 [μm]) used for these measurements is also shown. **(b)** Raman spectra measured in these zones, where two main peaks can be observed. A smoothing fit (white line over the black spectrum) was used to define the main characteristic peaks for the case of non-dewetted zones.

Appendix C: Reproducibility and stability of SERS measurements in MB-functionalized annealed Ag films.

The upper picture in **Fig. C(a)** shows each one of the four samples considered for studying the substrate aging effects in annealed films. As stated in the main text, a total of 20 measurements per aging instance were carried out (5 measurements on each of the 4 square films in the 2 x 2 array) in random branched zones. The raw spectra are shown in **Fig. C(a)**. Raman measurements carried out during a particular aging instance (1, 2, 3 or 4 weeks) present considerable dispersion. Nevertheless, the spectra were very similar in terms of signal/noise ratios and peak resolution, providing the same spectral information in each case. This fact is clarified by the example shown **Fig. C(b)**, which shows the normalized Raman spectra for the sample functionalized after 1 week of aging. In all the other cases, the conclusion was the same.
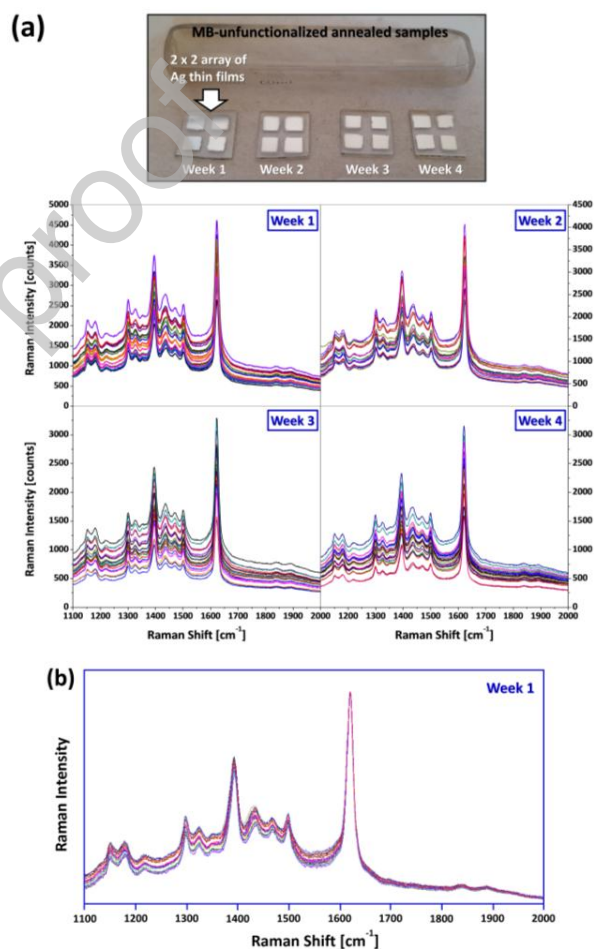

Fig. C.(a) Different Raman spectra measured for each aging instance in random branched channels. 20 measurement per instance were considered to have a statistical representation of the system behavior. **(b)** Normalized Raman spectra measured for the annealed sample with 1 week of aging. The Raman counts of the most intense peak at 1623 [cm^{-1}] for each spectrum was taken as reference value to perform the normalization.

11

Credit Author Statement

Simón Roa: Conceptualization, Validation, Formal analysis, Investigation, Writing - Original Draft, Writing - Review & Editing, Visualization, Project administration.

María José Cortés: Methodology, Investigation, Writing - Review & Editing, Visualization.

María Laura Pedano: Formal analysis, Investigation, Writing - Review & Editing, Visualization.

Graphical abstract
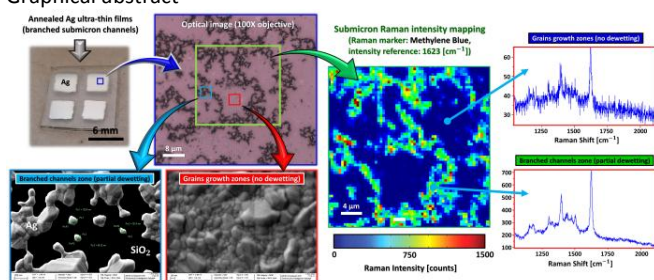
Declaration of interests

☒ The authors declare that they have no known competing financial interests or personal relationships that could have appeared to influence the work reported in this paper.

☐The authors declare the following financial interests/personal relationships which may be considered as potential competing interests: